DciA, the Bacterial Replicative Helicase Loader, promotes LLPS in the presence of ssDNA

Stéphanie Marsin, Sylvain Jeannin, Sonia Baconnais, Hélène Walbott, Gérard Péhau-arnaudet, Magali Noiray, Magali Aumont-Nicaise, Emil Gp Stender, Claire Cargemel, Romain Le Bars, et al.

Journal Pre-proofs

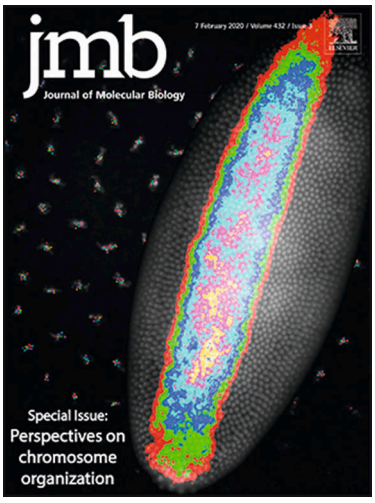

Research Article

DciA, the Bacterial Replicative Helicase Loader, promotes LLPS in the presence of ssDNA

Stéphanie Marsin, Sylvain Jeannin, Sonia Baconnais, Hélène Walbott, Gérard Pehau-Arnaudet, Magali Noiray, Magali Aumont-Nicaise, Emil GP Stender, Claire Cargemel, Romain Le Bars, Eric Le Cam, Sophie Quevillon-Cheruel

PII: S0022-2836(24)00503-5
DOI: https://doi.org/10.1016/j.jmb.2024.168873
Reference: YJMBI 168873

To appear in: *Journal of Molecular Biology*

Received Date: 28 June 2024
Revised Date: 15 November 2024
Accepted Date: 18 November 2024

Please cite this article as: S. Marsin, S. Jeannin, S. Baconnais, H. Walbott, G. Pehau-Arnaudet, M. Noiray, M. Aumont-Nicaise, E. GP Stender, C. Cargemel, R. Le Bars, E. Le Cam, S. Quevillon-Cheruel, DciA, the Bacterial Replicative Helicase Loader, promotes LLPS in the presence of ssDNA, *Journal of Molecular Biology* (2024), doi: https://doi.org/10.1016/j.jmb.2024.168873

DciA, the Bacterial Replicative Helicase Loader, promotes LLPS in the presence of ssDNA.

Stéphanie Marsin[1¶], Sylvain Jeannin[1], Sonia Baconnais[2], Hélène Walbott[1], Gérard Pehau-Arnaudet[3], Magali Noiray[1], Magali Aumont-Nicaise[1], Emil GP Stender[4], Claire Cargemel[1$], Romain Le Bars[1], Eric Le Cam[2], Sophie Quevillon-Cheruel[1¶]

[1] Université Paris-Saclay, CEA, CNRS, Institute for Integrative Biology of the Cell (I2BC), 91198, Gif-sur-Yvette, France.

[2] Genome Integrity and Cancer UMR 9019 CNRS, Université Paris-Saclay, Gustave Roussy 114 rue Edouard Vaillant, 94805 Villejuif, France.

[3] UTECH UBI, Institut Pasteur and CNRS UMR 3528, Paris, France.

[4] FIDA Biosystems Aps, Generatorvej 6 A+B, 2860 Søborg, Denmark.

[$] New address: Centre de Biologie Structurale (CBS), Université Montpellier, CNRS, INSERM, Montpellier, France

[¶]Correspondence: stephanie.marsin@i2bc.paris-saclay.fr and sophie.quevillon-cheruel@i2bc.paris-saclay.

Graphical abstract

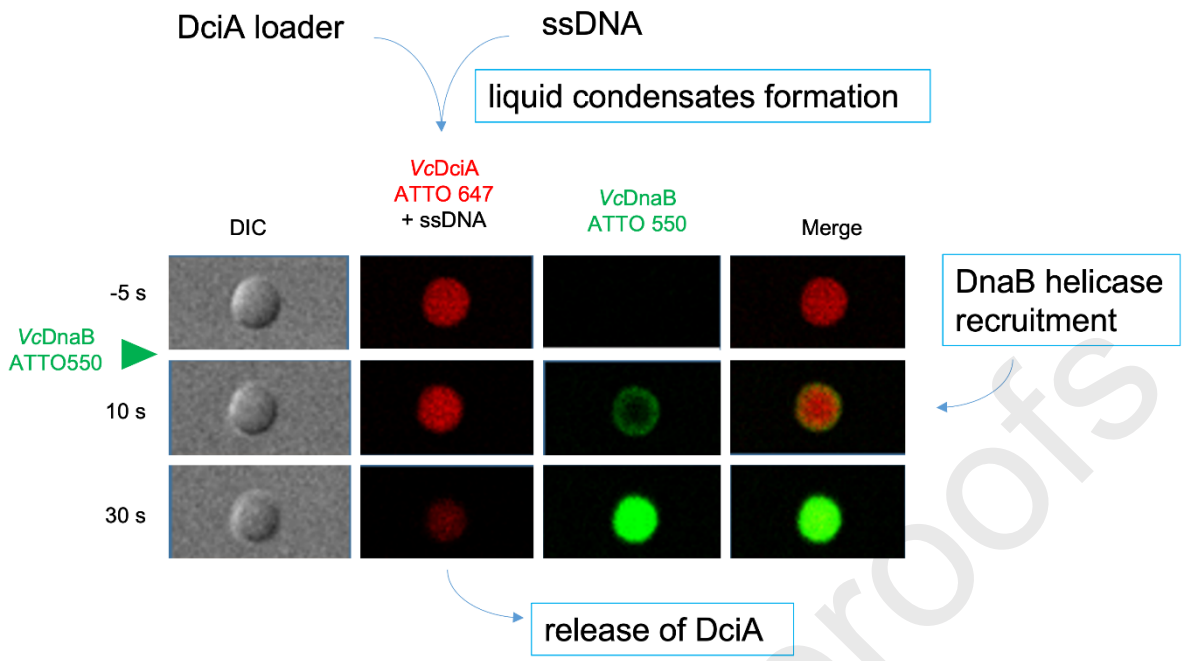

Research Highlights

The discovery that DciA, the loader of the bacterial replicative helicase, is capable of forming condensates in the presence of DNA, opens the way to the possibility of non-membrane compartments in bacteria, in order to concentrate the players involved in replication and thus facilitate it.

Abstract

The loading of the bacterial replicative helicase DnaB is an essential step for genome replication and depends on the assistance of accessory proteins. Several of these proteins have been identified across the bacterial phyla. DciA is the most common loading protein in bacteria, yet the one whose mechanism is the least understood. We have previously shown that DciA from *Vibrio cholerae* is composed of a globular domain followed by an unfolded extension and demonstrated its strong affinity for DNA. Here, we characterize the condensates formed by *Vc*DciA upon interaction with a short single-stranded DNA substrate. We demonstrate the fluidity of these condensates using light microscopy and address their network organization through electron microscopy, thereby bridging events to conclude on a liquid-liquid phase separation behavior. Additionally, we observe the recruitment of DnaB in the droplets, concomitant with the release of DciA. We show that the well-known helicase loader DnaC from *Escherichia coli* is also competent to form these phase-separated condensates in the presence of ssDNA. Our phenomenological data are still preliminary as

regards the existence of these condensates *in vivo*, but open the way for exploring the potential involvement of DciA in the formation of non-membrane compartments within the bacterium to facilitate the assembly of replication players on chromosomal DNA.

Keywords

DciA helicase loader, replicative helicase DnaB, protein-DNA condensates, LLPS

Introduction

Replicative helicases are essential proteins implicated in DNA replication in all kingdoms of life. They unwind the DNA double helix in front of the replisome, a large multi-subunit complex in charge of DNA strand synthesis [1], allowing its progression through the course of chromosome replication. Replisome assembly is tightly regulated, and the recruitment and loading of the replicative helicases on DNA is a key step in this mechanism [2, 3].

In bacteria, the loading of the closed and circular hexameric helicase DnaB depends on the intervention of loading proteins. In *Escherichia coli* (*Ec*), DnaC, a member of the ATPase Associated with various cellular Activities (AAA+) superfamily [4, 5], interacts with the LH/DH (Linker and Determinant Helices) module of the C-terminal ring of DnaB as a hexamer. This interaction causes a torsion to the closed ring formed by DnaB, cracking it open into a loading-competent state enabling the loading of the helicase on *oriC* [6-9]. In *Bacillus subtilis*, the other bacterial model studied closely, DnaI, a homolog of DnaC, has been described as a ring-maker but the molecular mechanism remains to be determined [10]. However, DnaC and DnaI are poorly represented in the bacterial world. Indeed, it has been shown in 2016 that the genes encoding these proteins were acquired by horizontal transfer from phage genomes [11, 12] and that the ancestral gene, replaced in these phyla by DnaC/I, encodes the protein DciA. Using DciA and DnaB from *Vibrio cholerae* (*Vc*) as models, and by comparison with the *E. coli* system, we previously demonstrated by biochemistry experiments supplemented by a structural study that DciA is indeed the helicase loader in this organism [13, 14].

*Vc*DciA is a small protein of 18 kDa containing a high level of arginine and lysine residues (13 R and 13 K over 158 residues), which gives it an isoelectric point of around 10. Structural analysis by NMR revealed that the N-terminal domain of *Vc*DciA is folded as a K-homology (KH) domain [11, 13, 15], described in the literature to interact with nucleic acids [16]. *Vc*DciA can indeed interact with single and double-stranded DNA, with a preference for the junction between these two structures, as we have previously shown by NMR and electron microscopy [17, 18]. The C-terminal domain remains unfolded [19] but adopts two small α-helices upon interacting with the LH/DH module of DnaB, without, however, exerting the torsional force observed with *Ec*DnaC on *Ec*DnaB [14]. Furthermore, we observed that, in contrast to *Ec*DnaC, *Vc*DciA is rapidly released from the helicase-DNA complex once the helicase is loaded onto DNA [13].

The precise mechanism of DnaB loading by DciA and the steps leading to this event remain to be elucidated. Given that the structure of the *Vc*DnaB•*Vc*DciA complex provides

limited insight into the loading-competent state, and there is no evidence supporting the ability of DciA to open the DnaB ring independently, we propose the involvement of an additional factor in the helicase loading mechanism. Considering DciA's affinity for DNA, we further explore how this molecule may contribute directly to the mechanism, beyond simply serving as a docking platform.

Over the past decade, numerous studies revealed the implication of membrane-less compartments in essential processes in cells. These condensates are mostly composed of DNA and proteins, and there is an increasing interest in understanding the role of biological condensates in these processes. The majority of observations have been made in eukaryotic cells, including the processes of DNA replication or DNA modulation by the topoisomerase [20, 21] among many other cellular functions. A growing number of studies also report the coordination of DNA Damage Response (DDR) with Liquid-Liquid Phase Separation (LLPS) processes [22]. A recent study described the phase separation properties of replication protein A (RPA), whose described function to protect ssDNA is now extended to genome organization and stability [23]. Numerous studies on viruses have also been published, revealing the importance of membrane-less replication compartments [24]. Some studies have been made in prokaryotes, where the idea of non-membrane compartmentalization allowing the concentration of proteins in specific sites of the cell via LLPS processes is advanced in different processes as varied as CO_2 concentration, transcription control, DNA segregation, RNA metabolism, or cell growth and division [25, 26]. Concerning DNA replication, repair, and recombination, it has been shown that the single-strand DNA binding protein SSB, the bacterial RPA analog, can produce phase separation via protein-protein interactions [27, 28].

To advance our understanding of the bacterial replicative helicase loading mechanism by the ancestral loader DciA, we investigated if DciA from *V. cholerae*, due to its appropriate biochemical properties, *i.e.* an intrinsically disordered region (IDR) in the C-terminal domain following a basic DNA-binding domain, was able *in vitro* to form condensates in the presence of ssDNA and characterized their liquid-like behavior. We then looked at whether these phase-separated droplets could play a role in the recruitment of the *Vc*DnaB helicase.

Results and Discussion

*Vc*DciA forms condensates in the presence of single-stranded DNA.

The first evidence that *Vc*DciA tended to form condensates was the results of crystallization trials performed with the purified protein. We have never been able to obtain *Vc*DciA crystals even at the highest protein concentration tested of 200 mg/mL (11 mM). Additionally, a larger-than-average number of crystallization drops showing phase separations were observed and appeared to be spherical structures. Secondly, during our previous studies, we often observed turbidity when *Vc*DciA was mixed with a single-stranded DNA (ssDNA).

We then explored these properties and established the optimal conditions to observe and study *Vc*DciA condensates. The turbidity of protein solutions containing *Vc*DciA at different concentrations was measured under different buffer and salt conditions

(Supplementary Fig. 1A). In MES buffer at pH6, with a NaCl concentration of 150 mM, mixing *Vc*DciA with an oligonucleotide (at 10 µM) results in suspension with high turbidity, due to the presence of droplets (Fig. 1A and Supplementary Fig. 1A). As a control, we observed no turbidity in the presence of DNA alone. With *Vc*DciA, at 300 mM of NaCl, the turbidity decreases drastically, suggesting that electrostatic forces are involved in droplets assembly (Supplementary Fig. 1A). No crowding agent like polyethylene glycol is required, and 10 µM of the protein is enough to observe the first signs of condensates. Turbidity was also observed in Hepes buffer and at pH7 (Supplementary Fig. 1A). We then validated the presence of *Vc*DciA and ssDNA in the droplets by using fluorescent labeling. Co-localization of *Vc*DciA, labeled with ATTO 550, and a 50-nucleotide long oligonucleotide labeled with Cy5 (ssDNA-Cy5) was observed, confirming their presence in the droplets (Fig. 1B). Knowing that potassium glutamate would be the more appropriate compound to test as it is the main salt in the cytoplasm of *E. coli* [28], we have performed turbidity experiments in this buffer (Supplementary Fig. 1A). We observed no difference in comparison with NaCl buffers, and we confirmed by confocal analysis droplet formation (Supplementary Fig. 1B). We have then chosen to use NaCl buffer, which we routinely use in the lab to measure protein-protein or nucleic acid interactions, or crystallogenesis.

On Pluronic pre-treated glass, we observed that condensates are not always spherical and spread out on the glass (Fig. 1B and Supplementary Fig. 1C). We then tested a silane coating to obtain a neutral surface, and observed that the condensates are indeed spherical even in the vertical axis, and do not wet the glass surface under these conditions (Fig. 1C and Supplementary Fig. 1D). We also observed that ssDNA-Cy5 rapidly penetrates preformed droplets composed of *Vc*DciA-ATTO 550 and unlabeled ssDNA (Fig. 1C). The fluorescent ssDNA can be detected at the periphery of the droplets 10 seconds after its addition, and is fully integrated after 20 seconds, displaying a homogeneous distribution inside the droplets similar to that of *Vc*DciA-ATTO 550, illustrating its fast diffusion.

ssDNA and *Vc*DciA are both required for condensate formation. Furthermore, the six histidines that form the N-terminal tag of *Vc*DciA are not involved in their formation, as untagged *Vc*DciA is also capable of forming similar condensates (Supplementary Fig. 2). These results are similar with that of ssDNA binding protein RPA [23], and additional experiments were conducted to confirm the liquid-like properties of the *Vc*DciA-ssDNA condensates.

Microscopy analysis of the *Vc*DciA-ssDNA condensates reveals liquid-like behavior.

To confirm the liquid-like material properties of the condensates, we investigated both their fusion abilities and the diffusion properties of the molecules within them. The first characteristic of condensates is their ability to fuse. Numerous events of droplet fusion were observed under the microscope (Supplementary Fig. 1E). The fusions occur in less than 5 seconds (time between two consecutive images) so we followed the fusion of two droplets labeled by different fluorescent tags: ATTO 550 and Cy5 (Fig. 2A). First, we induced condensates formation with *Vc*DciA labeled with ATTO 550 using its His-Tag (see Material and Methods), and unlabeled ssDNA (Fig. 2A -5 s). Then we added a suspension of preformed droplets containing unlabeled *Vc*DciA and ssDNA-Cy5 on the glass slide (Fig. 2A). At 133 seconds, we can see the early steps of the fusion event between an ATTO 550-labeled droplet

and a preformed droplet labeled with Cy5 (Fig. 2A in the circle). The size of the condensates increases, as shown in the dotted circle in the DIC (differential interference contrast) channel (Fig. 2A), but the two colors remain distinct. 5 seconds later (time = 138 s), the two droplets co-localize and the fusion is achieved. Colors merge totally in the next image, 5 seconds later. On the same field of view, at 174 seconds, two smallest droplets are present (in the dotted rectangle Fig. 2A). One was preformed and only labeled by ATTO 550, while the left one, coming from an out-of-focus plane, is already labeled by both ATTO 550 and Cy5, probably due to a previous fusion event. The two droplets fuse together and relax into one single spherical droplet. These observations confirm the liquid-like behavior of *Vc*DciA-ssDNA droplets. It was also possible to observe fusion events between two proximal droplets already installed on the glass (Supplementary Fig. 1E).

To further demonstrate the liquid-like dynamics of the *Vc*DciA droplets, we performed Fluorescence Recovery After Photobleaching (FRAP) experiments on *Vc*DciA labeled with ATTO 550 (Fig. 2B). *Vc*DciA exhibits fast dynamics with a nearly complete recovery after 1 minute of imaging: the mobile fraction represents 97.30±11%, with a half-time recovery $\tau\frac{1}{2}$= 6.81±1.9 seconds for a bleach spot of 1 µm diameter (Fig. 2C). Such a diffusion rate is consistent with those of other membrane-less organelles, such as nuclear speckles and nucleoli [29, 30].

For a better understanding of the DNA-protein interactions inside the droplets, we performed FRAP experiments on both ssDNA-Cy5 and *Vc*DciA-ATTO 550 at the same time. The ssDNA-Cy5 also showed a fast recovery, however, this recovery was significantly slower $\tau\frac{1}{2}$= 49.88±20 s and less complete than *Vc*DciA (only 76.18±16% after three minutes) (Supplementary Fig. 3A and 3B). If we compare for each experiment the $\tau\frac{1}{2}$ for *VcDciA* and ssDNA, we quantified that the DNA mobility is 3.6 fold slower than the *Vc*DciA protein (Supplementary Fig. 3C). We cannot rule out the possibility that this variation in mobility is due to a difference in charge and/or shape between DNA and *Vc*DciA. However, recovery of the DNA fluorescence confirms that it evolves in liquid droplets.

CapFlex (FIDA) analysis of condensates confirmed the importance of *Vc*DciA and DNA concentrations.

For further comprehension of *Vc*DciA-ssDNA droplets formation, we analyzed the droplets in different conditions with a FIDA (Flow-Induced Dispersion Analysis) device. CapFlex was recently used for the thermodynamic and kinetic characterization of protein droplets [31]. In these experiments, samples flowed through a capillary. When a droplet passes the detector, it will register a spike signal (see Materials and Methods). Thus, the number of spikes is correlated to the total number of droplets, and the signal intensity of the spikes is proportional to the size of the droplets. It should be noted that the proportion of free and *Vc*DciA-bound Ni-NTA-ATTO 488 probe inside and outside the droplets is not known, due to the non-covalent link between the probe and the His-Tag of *Vc*DciA. However, the increase in spike intensity confirms that both *Vc*DciA and the Ni-NTA-ATTO 488 probe enter the droplets (Fig. 3A). In this assay and due to the non-covalent labeling, the degree of phase separation is quantified solely by the number of spikes and their relative intensity and not the baseline intensity as

demonstrated by Stender *et al.* [31]. Therefore, the partitioning of the label into the droplets should not impact the conclusion.

Using this technology, we tried to see the droplets formation as a function of time and protein concentration, in similar experimental conditions as we observed the droplets under the microscope. We first made experiments at a fixed concentration of ssDNA (10 µM), with increasing concentrations of *Vc*DciA (Fig. 3A-C). Droplets were analyzed in triplicates. We can see that the spikes, almost absent at 10 µM of *Vc*DciA, increase in intensity depending on the concentration of *Vc*DciA, *i.e.* the peaks are higher at 30 µM than at 20 µM (Fig. 3A and 3C). But from 15 µM upwards, their number remains very stable despite the increase of the protein concentration (Fig. 3B). This suggests that beyond a certain concentration of *Vc*DciA, the formation of new droplets halts. The observation of the spreading of the droplet intensity distribution (Fig. 3C) might indicate an increase of the droplets size, but we cannot exclude the possibility that it could also signify an increase in the concentration of labeled *Vc*DciA inside the droplets [31].

The increased size of the droplets is concordant with what we observed in the photonic microscopy experiments: larger droplets can be observed as the concentration of *Vc*DciA increases. This phenomenon was even more obvious if we let them settle for 1 hour, probably due to the additional effect of droplet fusion and droplet growth (Fig. 2A and Supplementary Fig. 1E).

The impact of the DNA in the formation of the droplets has been studied by maintaining the *Vc*DciA concentration constant at 20 µM and by varying the concentration of the ssDNA (Fig. 3D). We confirmed that droplets formation is strictly dependent on DNA because there are no spikes in the absence of DNA, but that little DNA is needed (2 µM) to reach a large number of spikes. The number of spikes varies only marginally afterward, when the DNA concentration is increased.

TEM and cryoEM analysis of *Vc*DciA-ssDNA complexes: from networks to droplets formation

Our previous EM analysis of *Vc*DciA/DNA interactions, even at low protein concentration, suggested properties of *Vc*DciA to condense ssDNA [17]. We have explored these properties with 50 nucleotides long poly-dT and with large circular ssDNA provided from virion PhiX174 (5386 bases in length), which also allows *Vc*DciA to form droplets that can fuse as visualized by light microscopy (Supplementary Fig. 4). The use of short oligonucleotide informs on a global effect in this LLPS context and large ssDNA fragments allow to characterize the mechanisms involved in condensation. Both show that we are in the presence of a LLPS formation mechanism based on DNA-protein interactions. The positive staining associated with the darkfield image mode is a powerful and relevant method to analyze such behavior in equilibrium states for each condition, as previously shown for HIV nucleo-capsid protein [32] and confirmed as LLPS [33]. These complexes were visualized in parallel with negative staining.

*Vc*DciA:poly-dT50 complexes form small uneven spheres for 250 nM *Vc*DciA and 1.5 nM poly-dT50. Their sizes increase from 20 to 50 nm for 250 or 500 nM *Vc*DciA (Fig. 4A a1-4, b1-4) to 200 nm and more for 1 and 2 µM *Vc*DciA (Fig. 4A c-d). Although EM provides fixed

images, they correspond to equilibrium states for each condition. Some of these spheroids appear to grow by particle fusion mechanisms (Fig. 4A a2, b1, b3, c1, d1-3).

Interaction between PhiX174 ssDNA genome and *Vc*DciA leads to the formation of DNA networks at 250 nM *Vc*DciA as well as small spheroids (Fig. 4B b). These figures appear frequently under the same conditions (Fig. 4B c1-2), with structures of around 50 nm in diameter. Growth by fusion of these structures appears more clearly at 500 nM *Vc*DciA, producing spheroids of 50 to 200 nm (Fig. 4B d1-2). These growth mechanisms continue at 1 µM *Vc*DciA, where the structures appear irregularly shaped (Fig. 4B e1-2), whereas at 2 µM *Vc*DciA the shapes become more regular, with sizes of the order of 200 nm and more (Fig. 4B f1-3). We cannot exclude that the observed irregular shapes produce droplets in a reversible mechanism, ultimately allowing the formation of regular spheroids after further fusions.

EM allows us to characterize the formation and growth stages of these droplets, which occur from 250 nM *Vc*DciA upwards. With this technique, we can observe small droplets that are below the detection limit of fluorescence microscopy. We clearly show that such condensation results from network formation induced by bridging events, probably mediated by “DNA-protein”-“protein-DNA” interactions (Fig. 4B b, d1-2, f3). It is important to note that observations become unfeasible at concentrations exceeding 2 µM, due to the inability of the carbon support to withstand the samples, likely resulting from the large size and mass of the deposited droplet. Consequently, we consider that fusion is clearly a plausible model to explain droplet growth. We have no evidence that other mechanisms, such as Ostwald ripening, or flocculation, could explain the changes in condensate size [34].

To achieve a more detailed characterization of these networks, we examined the structure of *Vc*DciA-poly-dT50 complexes using cryo-electron microscopy (Fig. 4C). The resulting images revealed spherical condensates ranging from 50 to 200 nm, displaying variability in both size and shape. The heterogeneous LLPS condensates appear to represent different stages of the condensation process, with initial irregular DNA networks giving rise to more compact spherical structures, which subsequently grow into larger aggregates through fusion with other spherical condensates.

_Vc_DnaB is recruited to the condensates, leading to the release of _Vc_DciA.

The formation of condensates by *Vc*DciA in the presence of ssDNA is similar to previous studies reported for replication initiation factors in eukaryotes [21, 35]. Indeed, it was demonstrated that the proteins involved in eukaryote replicative helicase loading, ORC, Cdc6, and Cdt1, contain intrinsically disordered regions (IDRs) that drive LLPS [35]. Although these proteins have no structural similarity with *Vc*DciA, their function is similar. It was also demonstrated that the replicative MCM helicase can be recruited into those droplets [35]. We then decided to investigate an analog function for *Vc*DciA.

We previously demonstrated by Surface Plasmon Resonance (SPR) and Bio-Layer Interferometry (BLI) that the loading on ssDNA of the replicative helicase DnaB, from *V. cholerae* as well as from *E. coli*, is increased by *Vc*DciA [13, 14]. We then tried to see if *Vc*DciA could recruit *Vc*DnaB into preformed droplets (Fig. 5A). We performed this experiment in the

presence of ATP and $MgCl_2$, which are required for helicase hexamerization and activity [13, 36].

We first formed droplets with *Vc*DciA labeled with ATTO 647 and ssDNA (unlabeled), before adding (at t = 0 second in Fig. 5A) *Vc*DnaB labeled with ATTO 550. We observed that *Vc*DnaB-ATTO 550 rapidly localizes to the droplet periphery and is then quickly fully internalized. In Fig. 5B, we quantified the normalized droplet intensity for both labels. This approach confirmed that the fluorescence intensity of *Vc*DnaB-ATTO 550 starts to increase progressively inside the droplets 15 seconds after its addition, and reaches a plateau after 40 seconds. At the same time, *Vc*DciA-ATTO 647 signal inside the droplets decreases in inverse proportion to the increase in *Vc*DnaB. This suggests a competitive sequential recruitment of *Vc*DciA and *Vc*DnaB on DNA. In such a process, the dynamic behavior of the phase separation compartments seems critical for the displacement of VcDciA after the addition of *Vc*DnaB, leading to an exchange mechanism within the droplets in favor of *Vc*DnaB. As ATP and Mg^{2+} are present in the buffer, the helicase, once loaded onto the DNA, must translocate and displace *Vc*DciA. At 100 seconds, the droplets start to vanish: in DIC we observe that the contrast decreases drastically and that numerous small satellite objects appear, in the same time the fluorescence of *Vc*DnaB-ATTO 550 is also declining but still distinguishable in the previously described small satellite objects (Fig. 5A). To confirm that the fluorescent signal observed in the droplets is due to *Vc*DnaB-ATTO 550 presence and not the result of free dye binding to *Vc*DciA, we verified that Ni-NTA-ATTO 550, when added alone to *Vc*DciA-ssDNA droplets, is never recruited into the droplets (Supplementary Fig. 5A).

In the presence of *Vc*DnaB, the decrease of *Vc*DciA-ATTO 647 signal can be attributed to the fast release of *Vc*DciA from the DNA upon helicase loading onto it, as previously described in SPR assays [13]. This suggests that *Vc*DciA is in a second step released from the droplets by diffusion. Under the experimental conditions developed in this study, *Vc*DnaB-ATTO 550 alone is not visible since it remains soluble and does not form any condensate in the sole presence of ssDNA (Supplementary Fig. 5B). When we mixed *Vc*DnaB-ATTO 550 with *Vc*DciA-ATTO 647 and ssDNA, without first preforming the *Vc*DciA-ssDNA droplets, we observed undefined structures that could correspond to precipitates with both fluorescent tags inside (Supplementary Fig. 5C). This aggregation indicates that the proteins precipitate together in the presence of ssDNA in these conditions, as we have often observed when preparing the ternary complex samples for structural analysis by SAXS or crystallization. To this date, the underlying cause of this precipitation remains unknown. However, it is plausible that the simultaneous mixing of the three partners may hinder proper complex organization.

To control that the DNA remains present in the droplet after the arrival of *Vc*DnaB and the departure of *Vc*DciA, the same experiment was repeated, this time with droplets formed by unlabeled *Vc*DciA, in the presence of ssDNA-Cy5 before adding *Vc*DnaB-ATTO 550 (Supplementary Fig. 5D). We observed that *Vc*DnaB recruitment does not lead to DNA fluorescence disappearance at 30 seconds, whereas it was observed in Figure 5 that *Vc*DciA has already disappeared at this time.

*Ec*DnaC from *Escherichia coli* exhibits a behavior that closely resembles that of *Vc*DciA

There is no sequence or structural similarity between DciA and DnaC/I. While *Vc*DciA consists of a KH-like domain that binds nucleic acids [14], followed by a non-folded C-terminal extension that structures into 2 small α-helices upon contact with DnaB [14], *Ec*DnaC consists of an AAA+ domain preceded by a long α-helix that contacts DnaB [6]. Nevertheless, both loader proteins target the same surface on DnaB, the LH/DH module, which may allow us to qualify this similarity as an evolutionary convergence [14].

Here, we observed by light microscopy that droplets are formed when *Ec*DnaC and ssDNA are mixed under the protein/DNA concentration conditions established for *Vc*DciA, with both co-localizing within these droplets (Fig. 6A). We showed that there is indeed phase separation, but that the droplets generally appear smaller than those formed by *Vc*DciA-ssDNA (Supplementary Fig. 6A). Furthermore, we observed contacts between droplets that tend to end up in incomplete fusion events, or into droplets that do not relax into single spherical (homogenous) droplets (Supplementary Fig. 6B). The absence of fusion in droplets formed by *Ec*DnaC-ssDNA suggests that a process of liquid-to-solid transition in undergoing.

To better understand the nature of those droplets, we performed FRAP experiment in the same condition as for *Vc*DciA (Fig. 6B). Analysis of the FRAP experiments showed that only 26.68±12% of *Ec*DnaC-ATTO 550 associated fluorescence recovered after 1 minute, with a $\tau\frac{1}{2}$ of 47.2±16 s. This is much slower than the recovery observed for *Vc*DciA-ATTO 550. Moreover, the FRAP experiments on *Ec*DnaC-ATTO 550 showed a linear recovery of the fluorescence, which does reflect a LLPS behavior consistent with a high viscosity liquid. These observations suggest that *Ec*DnaC-ssDNA droplets do have not a fluid liquid-like nature but rather form gel-like objects. To gain more insight into the interactions inside *Ec*DnaC-ssDNA droplets, we performed again FRAP experiments on *Ec*DnaC-ATTO 550 and ssDNA-Cy5 at the same time on the same droplet with the same intensity (Supplementary Fig. 6C-D). The fluorescence recovery of ssDNA-Cy5 is still slower than *Ec*DnaC-ATTO 550 inside droplets as with *Vc*DciA-ssDNA condensates. This confirms the protein-ssDNA interactions inside the droplets. Nevertheless, the ssDNA has a mobile fraction of 24.6±6.7% with a $\tau\frac{1}{2}$ of 84.3±21 s which is even slower than in *Vc*DciA-ssDNA droplets. This is consistent with what we could expect inside gel-like droplets.

We were also able to observe the recruitment of *Ec*DnaB into the droplets, but with a much slower speed than in the case of *Vc*DciA-ssDNA droplets (Fig. 6C). While *Vc*DnaB is visible at the droplet periphery as early as 10 s, it takes over 1 min for *Ec*DnaB to appear at the periphery of *Ec*DnaC-ssDNA droplets. Moreover, it takes at least 340 s for *Ec*DnaB to be incorporated into the entire droplets (*vs* 20 s for *Vc*DnaB into the *Vc*DciA-ssDNA droplets), and no disappearance of *Ec*DnaC was observed up to 500 seconds, whereas *Vc*DciA was released in 50 seconds (compare Fig. 5A to Fig. 6C). Indeed, we observe only a slight decrease of the *Ec*DnaC-ATTO 550 fluorescence intensity inside the droplets (Fig. 6D). *Ec*DnaC-ssDNA droplets are probably in a more gel-like state, which may explain this difference in behavior, making them more persistent.

Conclusion

DciA is the replicative helicase loader predominantly found in the bacterial world. Contrary to what is known for DnaC, the loader that replaced DciA late in evolution [11], the mechanism that DciA applies to the helicase to ensure its loading onto DNA remains to be understood, as the structure of the *Vc*DnaB•*Vc*DciA complex that we have solved by crystallography shows no impact on the conformation of *Vc*DnaB by *Vc*DciA [13, 36] and therefore limits the molecular comprehension of DnaB loading. Thus, we have hypothesized that a further player is required to ensure this fundamental function and postulated that this other partner could be DNA itself.

*Vc*DciA, with a very electropositive overall charge, has the structural characteristics required for a DNA condenser: it is composed of a globular KH-type domain that we characterized as interacting with DNA [17], followed of an unfolded extension [17]. Hence, there is an interest in exploring the interplay between *Vc*DciA and DNA, as they possess the property of forming biomolecular condensates when put together. This paper is dedicated to the characterization of these droplets, using photonic and electron microscopy approaches. Considering that these condensates fulfill several characteristics such as circular shape, ability to fuse, sensitivity to ionic strength and fast recovery dynamics in FRAP experiments, we can assume that they are formed by a liquid-liquid phase separation mechanism [37]. We characterized their formation, their size and fluidity, and their capacity to recruit *Vc*DnaB.

Positive staining electron microscopy images, which provide a visualization of the ssDNA, and cryoEM analysis, provided evidence that the condensates we observed result from network formation, which we can assume is induced by bridging events. These bridges are presumed mediated by “DNA-protein”-“protein-DNA” interactions, and/or “protein-protein” interactions. These new data are consistent with the model we propose, that DciA may function as a chaperone for the DNA [17].

We showed that *Ec*DnaC also has the capacity to induce LLPS probably via interactions with DNA within droplets, although these are less fluid than those formed by *Vc*DciA as evidenced by the slower recovery dynamics in our FRAP experiments. The droplets formed by *Ec*DnaC seem to be smaller than those of *Vc*DciA, but the comparison is difficult due to different condensation points between the two loaders and less dynamic condensates for DnaC. This is probably also related to the inability of these objects to perform complete fusion events. However, despite the fact that DciA and DnaC are structurally unrelated, they are both capable of forming droplets in the presence of DNA. This sharing of physico-chemical properties raises the question of whether they might also share a common function *in vivo*. The question arises as to whether this ability of DciA and DnaC to form phase separation in the presence of ssDNA and to recruit the helicase into condensate has a biological relevance. Further investigations should be conducted to determine the biological significance of these findings. These include quantifying the abundance of DciA and DnaC proteins present in the cell, visualizing the colocalization of DnaB and DciA within the cell as foci, and identifying the involvement of other known replisome proteins, such as the Single-Stranded Binding (SSB) protein. Although our droplets reconstituted for the confocal microscopy experiments are often larger than a bacterium, the spheroids analyzed with nanometric EM resolution have sizes compatible with the bacterium diameter usually close to 1 µm. The low concentration of 250 nM of *Vc*DciA, sufficient to form droplets, suggests that these structures may exist *in vivo*. If this is indeed the case, which remains to be demonstrated since the sensitivity limits of the techniques we have employed do not allow us to simulate cell-like experimental conditions,

we can imagine that the aim could be to create a non-membrane compartment in the proximity of the *oriC* or arrested replication forks, to facilitate replication initiation and restart.

Materials and Methods

Oligonucleotides used

The poly-dT50 oligonucleotide (repetition of 50 thymines) was mixed with proteins for droplets formation observed by photonic microscopy. The ssDNA-Cy5, a 50 nucleotides long oligonucleotide named "Oso26" (5'-CCAGGAATACGGCAAGTTGGAGGCCGGGCTGGATGGAGACTAAGCTTTGG-3'), is labeled at its 5' extremity by a cyanine-5 (Cy5) and was mixed to follow DNA during fluorescent droplets imaging. A 50 nucleotides long oligo-dT is used for the electron microscopy experiments, as well as the ssDNA of the PhiX174 genome (New England Biolabs).

Protein samples preparation

*Vc*DnaB, *Ec*DnaC and *Ec*DnaB were all 6His-tagged at the C-terminus during the cloning process while *Vc*DciA is tagged at the N-terminus. After over-expressed in the *E. coli* Rosetta(DE3)pLysS or the BL21-Gold(DE3) strains, they were purified as described previously [13, 36]. Briefly, lysis were performed in buffer A (NaCl 200 mM, Tris–HCl 20 mM (pH7.5)) by sonication and the His-tagged proteins were purified on a Ni-NTA column (Qiagen Inc.), eluted with imidazole in buffer A but complemented by ATP 1 mM + $MgCl_2$ 3 mM in the case of the *Vibrio cholerae* helicase. *Vc*DciA or *Ec*DnaC were then loaded onto a Heparin column in a phosphate buffer (NH2PO4 20 mM, NaCl 100 mM (pH5.8)) and eluted with a gradient of NaCl (from 0.1 to 1.5 M). The two helicases were loaded onto a Superdex TM200 column 16/600 (GE), equilibrated against NaCl 100 mM, Tris–HCl 20 mM (pH8.8), complemented by ATP 1 mM, $MgCl_2$ 3 mM in the case of *Vc*DnaB. Their purification was completed with a MonoQ column (Amersham Pharmacia Biotech) in Tris–HCl (20 mM, pH8.8) and a gradient of NaCl (from 0.1 to 1 M). The proteins were flash frozen in liquid nitrogen and stored at -80°C. The level of purity of concentrated and stored protein samples is estimated on SDS-PAGE gel (Supplementary Fig. 7).

Turbidity analysis of droplets formation

Droplets were monitored by turbidity (optical density at 620 nm) by an Infinite-200-PRO-Fluorimeter (Tecan, Mannedorf, Switzerland). Analysis was performed at 30°C in 50 µl of the indicated buffer. Protein concentrations are indicated in the figures.

Protein Labelling for microscopy imaging

His-tagged proteins were labeled using Ni-NTA-ATTO 550 or Ni-NTA-ATTO 647 from Merck Group. Proteins at a final concentration of 300 µM were incubated 15 minutes on ice in 20 µl of MN buffer (50 mM MES pH6, 150 mM NaCl) with the indicated dye at a concentration of 30 µM (ratio dye/protein of 1/10).

Glass treatment for droplets Microscopy Imaging

Two kinds of coating were tested for droplets visualization at 25°C: Pluronic or neutral coating (siliconizing). For Pluronic coating, glass surfaces were treated by adding a filtered 10% solution of Pluronic F-127 and incubated for ~1h. The chambers were rinsed 5 times with MilliQ water and remained immersed in water until use. For neutral coating, glass surfaces were treated first with siliconizing solution Sigmacote (from Sigma) for 20 seconds, washed 5 times with MilliQ water, and treated after with Pluronic as in the case of Pluronic coating.

DIC and Fluorescent Microscopy Imaging

Droplets of protein were formed in MN buffer with 10 µM of a poly-dT50 oligonucleotide at 25°C. Samples (20 µl) were loaded on a µ-Slide 18 Well Glass Bottom (Ibidi, GMBH). Images were acquired on a LEICA SP8X inverted confocal laser scanning microscope equipped with a 63x HC Plan Apochromat CS2 oil-immersion objective (NA: 1.4) (Leica) with hybrid GaAsP detectors (Hamamatsu). For DIC images, we used the 481 nm wavelength. A white light laser was used to excite ATTO 550 at 550 nm and both ATTO 647 and Cy5 at 648 nm. The fluorescence is collected between 560 and 601 nm for ATTO 550, and between 675 and 726 nm for both ATTO 647 and Cy5. Image treatment and analysis were performed using FIJI free software [38].

FRAP experiments

FRAP acquisitions were performed at 25°C on an inverted Eclipse Ti-E (Nikon) microscope coupled with a CSU-X1-A1 Spinning Disk (Yokogawa), a 100x Apochromat TIRF oil immersion objective (NA: 1.49) (Nikon) and a Prime 95B sCMOS camera (Photometrics). The whole system is driven by MetaMorph software version 7.7 (Molecular Devices), and iLas 2 module (GATACA Systems) for FRAP.

All the bleaching events are performed in a circular region with a diameter of 1 µm and monitored over time for fluorescence recovery using a Quad band 440/40 nm, 521/20 nm, 607/34 nm, 700/45 nm emission filter (Semrock). For the *Vc*DciA-ATTO 550 FRAP experiment, we used the 561 nm, 100 mW laser (Coherent) set at 4% for the imaging and 44% for the bleaching, with an exposure time of 200 ms. The FRAP sequence was composed of a short pre-

bleach sequence of 3-5 s (1 image/s), the bleaching event, 2 successive post-bleach sequences of 20 s (2 images/s), and then a last sequence of variable length (1 image/s).

For the dual colors FRAP we adjusted the laser power to obtain similar bleaching amplitude in both channels (but this adjustment induces a variability between the recovery of the experiments done with one color than those done with 2 colors as the intensity is not the same). To get rid of most of the manipulation errors, we FRAP the DNA marked and *Vc*DciA marked at the same time on the same droplets and then calculated the ratio between each half-time recovery $\tau\frac{1}{2}$. To avoid acquisition-related bleaching, ssDNA is acquired at a frequency 5 times lower than that used for the protein, and the exposure time was 200 ms for *Vc*DciA and 100 ms for the ssDNA. The FRAP sequence was composed of : 5 s pre-bleach (1 image/s), bleaching event (150 ms), 2 successive post-bleach sequences of 20 s (1 image/s), and then 180 s (1 image/3 s).

FRAP curves were independently corrected and processed to obtain a double normalization as follow: the mean intensity of every bleached region was measured and the background intensity was subtracted by measuring a region outside the droplet. Acquisition-related bleaching correction is performed by dividing values by the whole droplet fluorescence intensity (as the bleached region can not be considered negligible). Then to display the recovery curves from 0 to 1, a double normalization is performed using the average of the pre-bleached signal and the 1st post-bleached value.

The mean indicated in the figures is the one calculated from all the measurements pooled. A custom-built macro was written in ImageJ to perform quantitative image analysis. As the recovery curves display a biphasic aspect, the mean curve was fitted by a double exponential function to extract both half-time recovery $\tau\frac{1}{2}$ and the mobile fraction.

When we were able to image and record the recovery to the plateau, the value of the plateau after fitting was used for the calculations. Otherwise, when the plateau was not achieved, we used the last recorded value to avoid fitting artifacts at the infinity.

FIDA experiments

For FIDA analysis, His tagged proteins were labeled using Ni-NTA-ATTO 488 (Merck Group) at a ratio of ATTO/protein = 1/500 in MN buffer.

Capflex was performed with a non-covalent Probe Ni-NTA-ATTO 488 complexed to *Vc*DciA unlike the covalent labels used before [26]. This means that the baseline corresponds to the concentration of Probe Ni-NTA-ATTO 488 in the dilute phase and not necessarily to *Vc*DciA. However, the label still enters the droplets and the signal can thus be used as a means of quantification. The Capflex method was described in detail previously [31]. Briefly, a sample is flowed through a capillary of 1 mm with an inner diameter of 75 µm. The auto-sampler and the capillary chamber is temperature controlled to a precision of 0.1 °C. As the sample passes the confocal fluorescence detector the baseline corresponds to the dilute phase concentration of the fluorescent probe and if the fluorescent probe enters the droplets, each time a droplet

passes the detection window a spike is observed. This means the total number of spikes correlates to the total number of droplets [31].

For the measurements of droplet formation, protein samples were prepared in MNP buffer (50 mM MES pH6, 150 mM NaCl, 0.1% Pluronic F-127) containing or not poly-dT50 nt single-stranded oligonucleotide. Proteins at the indicated concentration were incubated in the sample trays at 25 °C, and the capillary chamber was kept at 25 °C. A standard capillary with an inner diameter of 75 µm and a length of 1 mm was used. The following set of instrument parameters was used: wash with NaOH 1 M for 120 s at 3500 mbar; equilibration with MNP buffer for 120 s at 3500 mbar; sample analysis in MNP buffer with or without DNA during 240 s at 650 mbar. Between 3 and 11 replicates were launched, with 9 minutes intervals between each sample.

Automated baseline and peak height detection was done using a script running in Jupyter 6.1.4 (available here: DOI 10.11583/DTU.14223116). For a detailed description, please see [31].

Electron microscopy

TEM observations were carried out with a Zeiss 912AB transmission electron microscope in filtered zero-loss darkfield or brightfield imaging mode. Electron micrographs were obtained using a Tengra digital camera (Olympus) and a Soft Imaging Software system (iTEM).

The positive staining associated with darkfield filtered imaging mode is usually used to analyze nucleoprotein complexes containing large DNA molecules when negative staining and brightfield filtered imaging mode are dedicated to protein structure. For positive staining, 5 µl of different mixed are deposited on hexagonal 600 mesh copper grids, previously covered with a thin carbon film and functionalized in a homemade device by glow-discharge in the presence of amylamine, providing NH^{3+} charge deposition onto the carbon surface. For negative staining, 5 µl of different mixed were adsorbed onto a 300 mesh copper grid coated with a collodion film covered by a thin carbon film, activated by glow-discharge to make the carbon film hydrophilic. In both cases, after 1 min, grids were washed with aqueous 2% w/vol uranyl acetate (Merck, France) and then dried with ashless filter paper (VWR, France). The nucleo-complexes were reconstituted without incubation at room temperature by mixing 250 nM, 500 nM, 1 µM or 2 µM of *Vc*DciA with PhiX174 virion ssDNA or poly-dT50 oligonucleotides at a concentration of 1.5 µM nucleotides, in MN buffer.

Cryo-Electron microscopy

*Vc*DciA (14 µM) /poly-dT50 (10 µM) droplets were assembled at room temperature for 5 min in buffer (50 mM MES buffer (pH6) and 150 mM NaCl). After a dilution of 10 in buffer, 3 µl of the mix were deposited on glow-discharged Lacey grids (Agar Scientific) and cryo-fixed using an EMGP2 (Leica) which has the particularity to one-sided blot sample (humidity 100%, temperature 18°C, blot time 1 s). Grids were imaged on a Tecnai F20 microscope (Thermo

Fisher, USA) in low-dose conditions operating at 200 keV and using a Falcon II direct detector (Thermo Fisher, USA).

Acknowledgements

This work was supported by the French Infrastructure for Integrated Structural Biology (FRISBI) ANR-10-INBS-05, by funds from the Centre National de la Recherche Scientifique (CNRS), and by the Infrastructures en Biologie Santé et Agronomie (IBiSA). It has benefited from two I2BC facilities: Imagerie-Gif core facility, supported by the Agence Nationale de la Recherche (ANR-11-EQPX-0029/Morphoscope, ANR-10-INBS-04/FranceBioImaging; ANR-11-IDEX-0003-02/ Saclay Plant Sciences), and PIM facility supported by French Infrastructure for Integrated Structural Biology (FRISBI) (ANR-10-INBS-05). For cryoEM experiments, M. Nilges and the Equipex CACSICE (n° ANR-11-EQPX-0008) provided funding for the Falcon II direct detector. C.C. was supported by a Ph.D. fellowship from the French Ministry of Education.

Data availability

The authors declare that the data supporting the findings of this study are available within the article and its Supplementary Information files, or are available from the corresponding authors upon request.

Author contributions

S.M. and S.Q.-C. conceived this study; C.C., and S.Q.-C. purified the proteins; S.M., M.A-N. and M.N. performed the turbidity analysis; S.M., S.J. and R.L.B. performed the fluorescent microscopy imaging experiments; S.J. and R.L.B. performed the FRAP experiments; S.M. and E.GP.S. performed the FIDA experiments; E.L.C. and S.B. performed the electron microscopy experiments; S.B., H.W. and G.P-A. performed the cryo-electron microscopy experiments. S.M. and S.Q.-C. wrote the paper with input from all authors.

Declaration of generative AI and AI-assisted technologies in the writing process

During the preparation of this work the authors used ChatGPT in order to improve language and readability. After using this tool, the authors reviewed and edited the content as needed and take full responsibility for the content of the publication.

Figures legends

Figure 1: Photonic Microscopy images of condensates formed by *Vc*DciA and ssDNA

A. DIC images of *Vc*DciA in the presence of ssDNA. The droplets were formed with 15 µM of *Vc*DciA in the presence of 10 µM of poly-dT50 and loaded on glasses treated with Pluronic alone (see Materials and Methods). 5 µm scale is indicated.

B. Representative confocal images of *Vc*DciA labeled in the presence of fluorescent ssDNA. The droplets were formed with 15 µM of *Vc*DciA labeled with ATTO 550, in the presence of 10 µM of poly-dT50 and 0.2 µM of ssDNA labeled with Cy5 (ssDNA-Cy5). The droplets were loaded on glass treated with Pluronic alone (see Materials and Methods). 5 µm scale is indicated.

C. Microscope visualization of ssDNA integration into the droplets. The droplets were formed with 15 µM of *Vc*DciA labeled with ATTO 550, in the presence of 10 µM of poly-dT50, and 0.2 µM of ssDNA-Cy5 was added at the time indicated with the red arrow (between 0 and 10 s). Glasses were pre-treated with Sigmacote and Pluronic (see Materials and Methods). The most informative images are presented at 10 and 20 s. A 5 µm scale is indicated.

Figure 2: Analysis of *Vc*DciA condensates behavior by microscopy.

A. Fusion of *Vc*DciA droplets over time. The droplets were first formed with 30 µM of *Vc*DciA-ATTO 550 in the presence of 10 µM of poly-dT50 (-5 s). Pre-formed droplets, obtained as described above with 0.2 µM of ssDNA-Cy5, were then added at the time indicated by the red arrow (between 0 and 10 s). Images collected at indicated times were presented as they illustrated fusions between droplets of different colors. Dashed circles and rectangles indicate the fusion events of droplets. A 5 µm scale is indicated.

B. Representative time-lapse imaging of a FRAP experiment. The droplets were first formed with 30 µM of *Vc*DciA-ATTO 550 in the presence of 10 µM of poly-dT50. FRAP was applied on a central subregion (1 µm diameter). Time is indicated in seconds. The bleaching event is performed at time 0 s. The scale bar is 3 µm.

C. Quantification of recovery during FRAP experiments. Representation of the mean fluorescence intensity recovery of FRAP experiments presented in B (± standard deviation). Data were obtained from 3 independent replicates (n=34).

Figure 3: CapFlex (FIDA) analysis of the condensates.

A. Signal spikes observation. Three experiments are presented in the constant presence of poly-dT50 (10 µM) with *Vc*DciA at the indicated concentration. For each concentration, three measurements (triplicates) are reported with three different colors (blue, red, and green).

B. Spikes counting in various amounts of *Vc*DciA. Quantification of spikes number was performed on triplicate experiments and is reported for different *Vc*DciA concentrations, in the constant presence of poly-dT50 (10 µM).

C. Spikes intensity report in various amounts of *Vc*DciA. Each droplet intensity is presented for different *Vc*DciA concentrations.

D. Spikes counting in various amounts of ssDNA. Quantification of spikes number was performed on triplicate experiments and is reported for different poly-dT50 concentrations, in the constant presence of *Vc*DciA (20 µM).

Figure 4: Electron microscopy and cryoEM analysis of *Vc*DciA-ssDNA complexes.

A. Condensates formation in the presence of poly-dT50 oligonucleotide (1.5 µM), with 250 nM (a1-4), 500 nM (b1-4), 1 µM (c1-2) and 2 µM (d1-4) of *Vc*DciA. All complexes were obtained by positive staining method visualized in darkfield mode except a4, b4, d4 where samples were obtained by negative staining visualized in brightfield mode. The scale bar is 200 nm.

B. Condensates formation in the presence of PhiX174 virion ssDNA genome (1.5 µM) without (a) and with 250 nM (b, c1-2), 500 nM (d1-2), 1 µM (e1-2) and 2 µM (f1-3) of *Vc*DciA. All complexes were obtained by positive staining method visualized in darkfield mode. The scale bars are 200 nm and 100 nm for c1.

C. (a-d) CryoEM of condensates resulting from poly-dT50 (10 µM) – *Vc*DciA (14 µM) interactions. 50 nm scale is indicated.

Figure 5: *Vc*DciA recruits *Vc*DnaB into the condensates.

The condensates were formed with 12 µM of *Vc*DciA-ATTO 647 in the presence of 10 µM of poly-dT50 in MN buffer containing 1 mM ATP with 10 mM $MgCl_2$. Between 0 and 10 seconds, *Vc*DnaB-ATTO 550 was added at the final concentration of 4 µM.

A. Representative confocal images. Images collected at indicated times were presented as they illustrated the different events. 10 µm scale is indicated.

B. Quantification. Representative graphic of the average of the mean intensity (± standard deviation) within a droplet, normalized to 1. Full circles represent *Vc*DnaB-ATTO 550 and open circles *Vc*DciA-ATTO 647. The average was measured on n=6 distinct droplets.

Figure 6: Microscopy analysis of condensates formed by *Ec*DnaC.

A. Representative confocal image of labeled *Ec*DnaC in the presence of fluorescent ssDNA. The condensates were formed with 15 µM of *Ec*DnaC labeled with ATTO 550, in the presence of 10 µM of poly-dT50 and 0.2 µM of ssDNA labeled with Cy5 (ssDNA-Cy5). 5 µm scale is indicated.

B. FRAP experiments on *Ec*DnaC condensates. The condensates were first formed with 30 µM of *Ec*DnaC-ATTO 550 in the presence of 10 µM of poly-dT50. On top, representative time-lapse

imaging of a FRAP experiment. FRAP was applied on a central sub-region (1 µm diameter). Time is indicated in seconds. The bleaching event is performed at time 0 s. The scale bar is 3 µm. On the bottom part is a representation of the mean fluorescence intensity recovery (± standard deviation) of FRAP experiments presented on the top (full circles). Data were obtained from 3 independent replicates (n=25). The dotted line is a reminder of the mean *Vc*DciA recovery (shown in comparison).

C. *Ec*DnaC recruits *Ec*DnaB into the condensates. The condensates were formed with 12 µM of *Ec*DnaC-ATTO 647 in the presence of 10 µM of poly-dT50 in MN buffer containing 1 mM ATP with 10 mM $MgCl_2$. 10 µm scale is indicated. Between 0 and 10 seconds, *Ec*DnaB-ATTO 550 was added at the final concentration of 4 µM. Images collected at indicated times were presented as they illustrated the different events.

D. Quantification. Representative graphic of the average of the mean intensity (± standard deviation) within a droplet, normalized to 1. Full circles represent *Ec*DnaB-ATTO 550 and open circles *Ec*DnaC-ATTO 647.

References

1. Yao, N. & O'Donnell, M. (2016) Bacterial and Eukaryotic Replisome Machines, *JSM biochemistry and molecular biology.* **3**.

2. Soultanas, P. (2012) Loading mechanisms of ring helicases at replication origins, *Molecular microbiology.* **84**, 6-16.

3. Katayama, T., Ozaki, S., Keyamura, K. & Fujimitsu, K. (2010) Regulation of the replication cycle: conserved and diverse regulatory systems for DnaA and oriC, *Nature reviews Microbiology.* **8**, 163-70.

4. Mott, M. L. & Berger, J. M. (2007) DNA replication initiation: mechanisms and regulation in bacteria, *Nature reviews Microbiology.* **5**, 343-54.

5. Tsai, K. L., Lo, Y. H., Sun, Y. J. & Hsiao, C. D. (2009) Molecular interplay between the replicative helicase DnaC and its loader protein DnaI from Geobacillus kaustophilus, *Journal of molecular biology.* **393**, 1056-69.

6. Arias-Palomo, E., O'Shea, V. L., Hood, I. V. & Berger, J. M. (2013) The bacterial DnaC helicase loader is a DnaB ring breaker, *Cell.* **153**, 438-48.

7. Arias-Palomo, E., Puri, N., O'Shea Murray, V. L., Yan, Q. & Berger, J. M. (2019) Physical Basis for the Loading of a Bacterial Replicative Helicase onto DNA, *Molecular cell.* **74**, 173-184.e4.

8. Liu, B., Eliason, W. K. & Steitz, T. A. (2013) Structure of a helicase-helicase loader complex reveals insights into the mechanism of bacterial primosome assembly, *Nature Communications.* **4**, 2495.

9. Nagata, K., Okada, A., Ohtsuka, J., Ohkuri, T., Akama, Y., Sakiyama, Y., Miyazaki, E., Horita, S., Katayama, T., Ueda, T. & Tanokura, M. (2020) Crystal structure of the complex of the interaction domains of Escherichia coli DnaB helicase and DnaC helicase loader: structural basis implying a distortion-accumulation mechanism for the DnaB ring opening caused by DnaC binding, *Journal of biochemistry.* **167**, 1-14.

10. Velten, M., McGovern, S., Marsin, S., Ehrlich, S. D., Noirot, P. & Polard, P. (2003) A two-protein strategy for the functional loading of a cellular replicative DNA helicase, *Molecular cell.* **11**, 1009-20.

11. Brézellec, P., Vallet-Gely, I., Possoz, C., Quevillon-Cheruel, S. & Ferat, J. L. (2016) DciA is an ancestral replicative helicase operator essential for bacterial replication initiation, *Nature Communications.* **7**, 13271.

12. Brézellec, P., Petit, M. A., Pasek, S., Vallet-Gely, I., Possoz, C. & Ferat, J. L. (2017) Domestication of Lambda Phage Genes into a Putative Third Type of Replicative Helicase Matchmaker, *Genome Biology and Evolution.* **9**, 1561-6.

13. Marsin, S., Adam, Y., Cargemel, C., Andreani, J., Baconnais, S., Legrand, P., Li de la Sierra-Gallay, I., Humbert, A., Aumont-Nicaise, M., Velours, C., Ochsenbein, F., Durand, D., Le Cam, E., Walbott, H., Possoz, C., Quevillon-Cheruel, S. & Ferat, J. L. (2021) Study of the DnaB:DciA interplay reveals insights into the primary mode of loading of the bacterial replicative helicase, *Nucleic acids research.* **49**, 6569-6586.

14. Cargemel, C., Marsin, S., Noiray, M., Legrand, P., Bounoua, H., Li de la Sierra-Gallay, I., Walbott, H. & Quevillon-Cheruel, S. (2023) The LH-DH module of bacterial replicative helicases is the common binding site for DciA and other helicase loaders, *Acta crystallographica Section D, Structural biology.* **79**, 177-187.

15. Blaine, H. C., Burke, J. T., Ravi, J. & Stallings, C. L. (2022) DciA Helicase Operators Exhibit Diversity across Bacterial Phyla, *Journal of bacteriology.* **204**, e0016322.

16. Valverde, R., Edwards, L. & Regan, L. (2008) Structure and function of KH domains, *The FEBS journal.* **275**, 2712-26.

17. Cargemel, C., Baconnais, S., Aumont-Nicaise, M., Noiray, M., Maurin, L., Andreani, J., Walbott, H., Le Cam, E., Ochsenbein, F., Marsin, S. & Quevillon-Cheruel, S. (2023) Structural Insights of the DciA Helicase Loader in Its Relationship with DNA, *International journal of molecular sciences.* **24**.

18. Mann, K. M., Huang, D. L., Hooppaw, A. J., Logsdon, M. M., Richardson, K., Lee, H. J., Kimmey, J. M., Aldridge, B. B. & Stallings, C. L. (2017) Rv0004 is a new essential member of the mycobacterial DNA replication machinery, *PLoS genetics.* **13**, e1007115.

19. Chan-Yao-Chong, M., Marsin, S., Quevillon-Cheruel, S., Durand, D. & Ha-Duong, T. (2020) Structural ensemble and biological activity of DciA intrinsically disordered region, *Journal of structural biology.* **212**, 107573.

20. Jeong, J., Lee, J. H., Carcamo, C. C., Parker, M. W. & Berger, J. M. (2022) DNA-Stimulated Liquid-Liquid phase separation by eukaryotic topoisomerase ii modulates catalytic function, *eLife.* **11**.

21. Parker, M. W., Kao, J. A., Huang, A., Berger, J. M. & Botchan, M. R. (2021) Molecular determinants of phase separation for Drosophila DNA replication licensing factors, *eLife.* **10**.

22. Stanic, M. & Mekhail, K. (2022) Integration of DNA damage responses with dynamic spatial genome organization, *Trends in genetics : TIG.* **38**, 290-304.

23. Spegg, V., Panagopoulos, A., Stout, M., Krishnan, A., Reginato, G., Imhof, R., Roschitzki, B., Cejka, P. & Altmeyer, M. (2023) Phase separation properties of RPA combine high-affinity ssDNA binding with dynamic condensate functions at telomeres, *Nature structural & molecular biology.* **30**, 451-462.

24. Nevers, Q., Albertini, A. A., Lagaudrière-Gesbert, C. & Gaudin, Y. (2020) Negri bodies and other virus membrane-less replication compartments, *Biochimica et biophysica acta Molecular cell research.* **1867**, 118831.

25. Gao, Z., Zhang, W., Chang, R., Zhang, S., Yang, G. & Zhao, G. (2021) Liquid-Liquid Phase Separation: Unraveling the Enigma of Biomolecular Condensates in Microbial Cells, *Frontiers in microbiology.* **12**, 751880.

26. Guo, D., Xiong, Y., Fu, B., Sha, Z., Li, B. & Wu, H. (2024) Liquid-Liquid phase separation in bacteria, *Microbiological research.* **281**, 127627.

27. Harami, G. M., Kovács, Z. J., Pancsa, R., Pálinkás, J., Baráth, V., Tárnok, K., Málnási-Csizmadia, A. & Kovács, M. (2020) Phase separation by ssDNA binding protein controlled via protein−protein and protein−DNA interactions, *Proceedings of the National Academy of Sciences of the United States of America.* **117**, 26206-17.

28. Kozlov, A. G., Cheng, X., Zhang, H., Shinn, M. K., Weiland, E., Nguyen, B., Shkel, I. A., Zytkiewicz, E., Finkelstein, I. J., Record, M. T., Jr. & Lohman, T. M. (2022) How Glutamate Promotes Liquid-liquid Phase Separation and DNA Binding Cooperativity of E. coli SSB Protein, *Journal of molecular biology.* **434**, 167562.

29. Phair, R. D. & Misteli, T. (2000) High mobility of proteins in the mammalian cell nucleus, *Nature.* **404**, 604-9.

30. Molliex, A., Temirov, J., Lee, J., Coughlin, M., Kanagaraj, A. P., Kim, H. J., Mittag, T. & Taylor, J. P. (2015) Phase separation by low complexity domains promotes stress granule assembly and drives pathological fibrillization, *Cell.* **163**, 123-33.

31. Stender, E. G. P., Ray, S., Norrild, R. K., Larsen, J. A., Petersen, D., Farzadfard, A., Galvagnion, C., Jensen, H. & Buell, A. K. (2021) Capillary flow experiments for thermodynamic and kinetic characterization of protein liquid-liquid phase separation, *Nature Communications.* **12**, 7289.

32. Le Cam, E., Coulaud, D., Delain, E., Petitjean, P., Roques, B. P., Gérard, D., Stoylova, E., Vuilleumier, C., Stoylov, S. P. & Mély, Y. (1998) Properties and growth mechanism of the ordered aggregation of a model RNA by the HIV-1 nucleocapsid protein: an electron microscopy investigation, *Biopolymers.* **45**, 217-29.

33. Monette, A., Niu, M., Nijhoff Asser, M., Gorelick, R. J. & Mouland, A. J. (2022) Scaffolding viral protein NC nucleates phase separation of the HIV-1 biomolecular condensate, *Cell reports.* **40**, 111251.

34. Naz, M., Zhang, L., Chen, C., Yang, S., Dou, H., Mann, S. & Li, J. (2024) Self-assembly of stabilized droplets from liquid-liquid phase separation for higher-order structures and functions, *Communications chemistry.* **7**, 79.

35. Parker, M. W., Bell, M., Mir, M., Kao, J. A., Darzacq, X., Botchan, M. R. & Berger, J. M. (2019) A new class of disordered elements controls DNA replication through initiator self-assembly, *eLife.* **8**.

36. Cargemel, C., Walbott, H., Durand, D., Legrand, P., Ouldali, M., Ferat, J. L., Marsin, S. & Quevillon-Cheruel, S. (2022) The apo-form of the Vibrio cholerae replicative helicase DnaB is a labile and inactive planar trimer of dimers, *FEBS letters.* **596**, 2031-2040.

37. Alberti, S., Gladfelter, A. & Mittag, T. (2019) Considerations and Challenges in Studying Liquid-Liquid Phase Separation and Biomolecular Condensates, *Cell.* **176**, 419-434.

38. Schindelin, J., Arganda-Carreras, I., Frise, E., Kaynig, V., Longair, M., Pietzsch, T., Preibisch, S., Rueden, C., Saalfeld, S., Schmid, B., Tinevez, J. Y., White, D. J., Hartenstein, V., Eliceiri, K., Tomancak, P. & Cardona, A. (2012) Fiji: an open-source platform for biological-image analysis, *Nature methods.* **9**, 676-82.

Figure 1

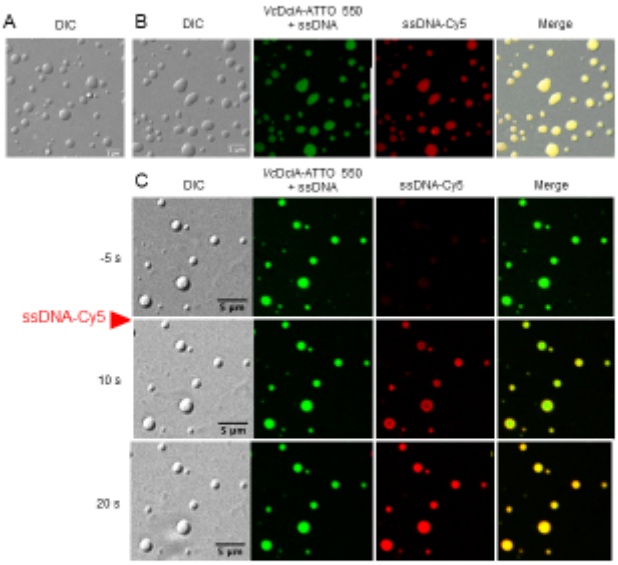

Figure 2

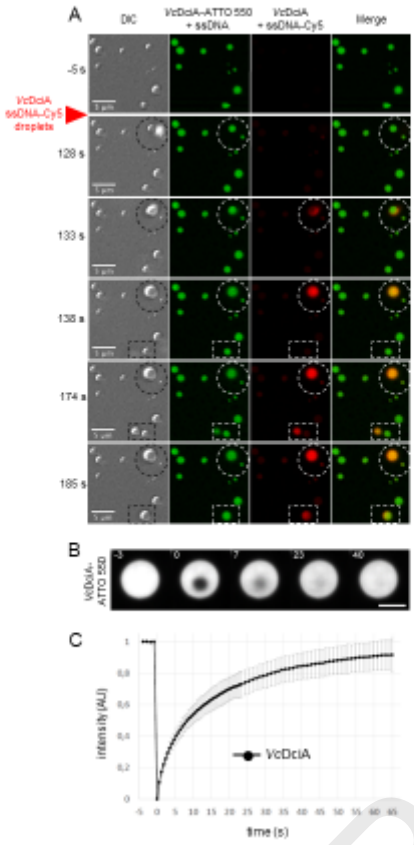

Figure 3

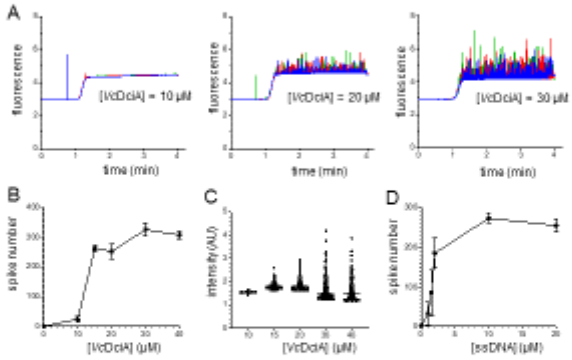

Figure 4

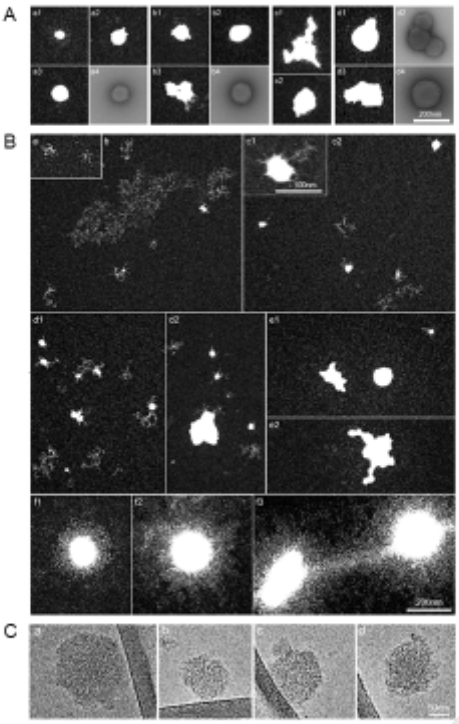

Figure 5

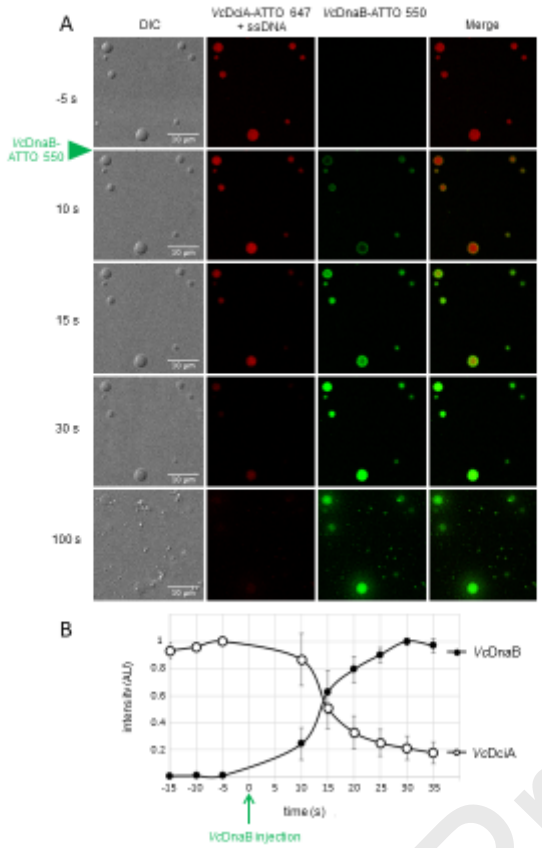

Figure 6

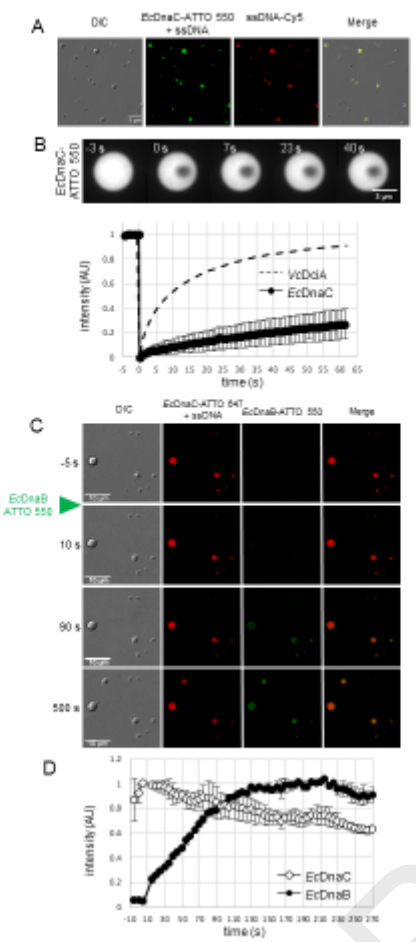

we declare that we have no conflict of interest